Extremely correlated Fermi liquids: Self-consistent solution of the second-order theory

Daniel Hansen and B. Sriram Shastry
Physics Department, University of California, Santa Cruz, California 95064, USA
(Received 5 November 2012; revised manuscript received 10 May 2013; published 6 June 2013)

We present detailed results from a recent microscopic theory of extremely correlated Fermi liquids, applied to the t-J model in two dimensions, developed recently by Shastry [Phys. Rev. Lett. **107**, 056403 (2011); Phys. Rev. B **87**, 125124 (2013)]. The second-order theory in the parameter λ, related to the density, is argued to be quantitatively valid in the overdoped regime for $0 \leqslant n \lesssim 0.75$, with n denoting the particle density. The calculation involves the self-consistent solution of equations for an auxiliary Fermi liquid Green's function and an adaptive spectral weight. We present numerical results at low as well as high T, at various low to intermediate densities in the normal phase, using a minimal set of band parameters relevant to the cuprate superconductors. We display the momentum space occupation function m_k, energy dispersion curves locating the peaks of spectral functions, the optical conductivity, relaxation rates for quasiparticles, and the electronic spectral functions on an *absolute scale*. The line shapes have an asymmetric shape and a broad background that is also seen in experiments, and our calculations validate approximate recent versions of the theory. The results also display the experimentally noted high-energy kink and provide an in-depth understanding of its origin and dependence on band parameters.

DOI: 10.1103/PhysRevB.87.245101 PACS number(s): 71.10.−w, 71.10.Fd

I. INTRODUCTION

The t-J model describes the physics of very strongly interacting electrons, made especially difficult by the requirement of (at most) single occupancy of the lattice sites. It is the subject of many recent works in the context of the cuprate superconductors, and also other correlated systems such as sodium cobaltates. This problem is very hard since it precludes the application of standard perturbative methods. This conundrum has motivated a new strong-coupling approach, resulting in the theory of *extremely correlated Fermi liquids* (ECFLs).[1,2] Previous applications of the methodology of Ref. 1 to the cuprates has given encouraging results. These include spectral functions that compare very well with the experimental angle-resolved photoemission spectroscopy (ARPES) data,[3–6] providing natural explanations of the "high-energy kink," and also the more subtle "low-energy kink" seen in experiments. The theory also has led to interesting predictions for the asymmetry of line shapes.[6]

The formalism initiated in Ref. 1 charted out an approach to the problem of the t-J model using basic insights from Schwinger's powerful approach to field theory, using source fields to write down exact functional differential equations for the propagator. In the next crucial step, it was recognized that complexity arising from the noncanonical nature of the (projected) electrons can be circumvented by a product *ansatz*. This involves decomposing the propagator as the space time convolution of a *canonical electron propagator*, and an adaptive spectral weight factor termed *the caparison factor* satisfying coupled equations of motion. A recent work[2] develops this idea in a systematic fashion, emphasizing the role of expanding in a parameter λ $(0 \leqslant \lambda \leqslant 1)$, related to the particle density, or more closely to $\lambda \sim (1 - \frac{4}{n^2} d)$, where d is the double occupancy $(0 \leqslant d \leqslant \frac{n^2}{4})$. It further explores the implications of a novel set of identities for the t-J model, termed the *shift identities*. These simple but crucial identities provide an important constraint on the λ expansion. A method for generating a systematic set of equations for the propagator to any orders in λ is given, along with explicit equations to second order in λ that manifestly obey the shift identity constraints. We will refer to this theory as (I) here and prefix equations of that paper with (I). A detailed numerical solution of this $O(\lambda^2)$ ECFL propagator is the main focus of this work. We obtained and benchmark the results of these equations against known results, and thereby provide a solid platform for further developments of the method, as well as a validation of the phenomenological versions of ECFL. With the confidence gained by the benchmarking, we further study and report the hopping parameter sensitivity of the kink effect.

Broadly speaking, the $O(\lambda^m)$ equations resemble the fully self-consistent mth-order skeleton diagram expansion of the standard Feynman-diagram-based theory, as described in standard texts,[7–9] but generalize to the case of extreme correlations. Summarizing the arguments in Refs. 1 and 2, a low-order theory in λ is already expected to capture features of extreme correlations. This perhaps initially surprising expectation arises in view of the non-Dysonian representation of the Green's function in terms of two self-energies Φ and Ψ, within the ECFL formalism. The self-energy Ψ resides in the numerator of the Green's function, as in Eqs. (1) and (2) . It plays the role of an adaptive spectral weight that balances the somewhat opposing requirements of the "high-energy" weight $1 - \frac{n}{2}$ and the low-energy Luttinger theorem. The latter requires a greater magnitude of the numerator than $1 - \frac{n}{2}$ to accommodate the particles into a Fermi surface (FS) with the same volume as in the Fermi gas. A further tactical advantage of this method is due to the finite range of variation of λ, namely, $0 \leqslant \lambda \leqslant 1$, that suffices to interpolate between the Fermi gas and the extreme correlation limit. This is in contrast to controlling the double occupancy d using a repulsive energy U, with its range of values $0 \leqslant U \leqslant \infty$. Experience shows that U must be tuned to a very large value $U \gg |t|$ in order to achieve the same end, thereby invalidating low-order expansions in U. In summary, within the present formalism, a low-order theory in λ seems well worth examining in detail; this is our task here.

We note that apart from a few exact solutions in one dimension and some calculations for finite-sized systems (see below), we are aware of no systematic analytical calculations in higher dimensions, for the dynamics of the physically relevant spin-$\frac{1}{2}$ version of the t-J model, working directly in the thermodynamic limit. An earlier body of work in Ref. 10 shares some of the objectives and features of our approach but is technically very different. It relies on an expansion in the inverse number of components $\frac{1}{\mathcal{N}}$ and is thus somewhat removed from the physical case of interest, where $\mathcal{N} = 2$. Therefore while the importance of the t-J model was understood many years ago, there has been little detailed comparison with the ARPES experiments until recently.[3,4] This gap is one of the main motivations for this (and our related) work. In this paper, we present a controlled calculation for the spectral functions of the t-J model by solving the above $O(\lambda^2)$ equations. We evaluate thermodynamical variables, the spectral functions, ARPES line shapes, and optical conductivity of the t-J model. The ECFL formalism and the λ expansion method provides an in-built criterion to judge the validity of the expansion at any order. Using this criterion we argue that our present $O(\lambda^2)$ calculations are valid in the high-hole-doping limit, known as the overdoped regime. Clearly this corresponds to low and intermediate *electron density*, since the hole doping is related to the particle density as $x = 1 - n$. Future work will be aimed at higher-order calculations in λ in order to enable us to address densities closer to optimal doping ($n \sim 0.85$). The results are compared with other approximations as well as a few experiments. Needless to say, even in such an overdoped regime, experimental evidence points to the important role of strong correlations.[11,12]

While analytical methods beyond crude mean-field theories have been in short supply, there is a valuable body of numerical results for the t-J model from exact diagonalization,[13] high-temperature series expansions,[14] variational wave functions,[15–17] and finite temperature Lanczos methods.[18–21] Noteworthy are the results of Ref. 19 from Prelovsek and co-workers, who handle the series expansion in inverse temperature in a stochastic fashion, thereby obtaining results down to fairly low temperatures. Owing to finite size effects and the inherent nature of the high-T expansion, the results from this theory, although broadly comparable to ours, seem more grainy.

The Hubbard model for large on-site coupling U tends to the t-J model [apart from $O(t^2/U)$ correction terms], so the large U studies of this model are of interest. Quantum Monte Carlo methods, despite the difficulties associated with the sign problem, yield some valuable insights into the spectral features such as kinks.[22] We note that the dynamical mean-field theory (DMFT) for the Hubbard model[23,24] gives a numerically exact solution in high enough dimensions of the Hubbard model. Although the strong coupling (i.e., $U > W$) relevant to the t-J model results is challenging, there is impressive progress overall. A recent DMFT study[25] at strong coupling obtains detailed spectral functions that are roughly comparable to what we find here for the t-J model.

The ECFL formalism has several advantages, since it is essentially an analytical method with a computational aspect that is lightweight, in comparison with other methods listed above. The only present limitation is the density attainable with the second-order theory. When possible, we present absolute scale results that are encouragingly close to experimental data with no other fitted parameters.

We finally note that the present $O(\lambda^2)$ results for the location of the energy peaks has been recently tested in Ref. 26, against an independent theory with overlapping validity. Reference 26 studied the infinite-coupling Hubbard model in two dimensions by using a highly efficient computer program to generate a series expansion in hopping of the exact Green's function and its various moments to high order. The locations of the dispersion peaks can be estimated from these. These dispersion relations match *quantitatively* the ones found from the present theory, with $J \to 0$ for the densities quoted in this paper. This suggests a high degree of reliability of the spectral functions discussed herein.

The plan of the paper is as follows: In Sec. II, we present a summary of the equations solved here from Sec. I. In Sec. III, we discuss the computational strategy and explain the scheme, using the fast Fourier transform method (FFT), so that the spectral functions can be computed efficiently. Section IV presents the detailed results of the calculation. Section V contains a summary and concluding comments. The Supplemental Material in Ref. 27 details the results for thermodynamics and the wave-function renormalization Z_k, and also gives further details of the computational method employed.

II. SUMMARY OF THE $O(\lambda^2)$ THEORY

In the ECFL formalism developed in (I) (i.e. Ref. 2), the physical Green's function $\mathcal{G}$ can be factored in the momentum space as

$$\mathcal{G}(k) = \mathbf{g}(k)\,\mu(k), \quad \text{where } (k) \equiv (\vec{k}, i\omega_k). \tag{1}$$

Here the caparison factor $\mu(k)$ plays the role of an adaptive spectral weight, while $\mathbf{g}(k)$ is the auxiliary canonical Fermion propagator. These objects are expanded in powers of a parameter λ, relating to density, and finally we set $\lambda \to 1$. As shown in Eqs. (I-83), (I-84), and (I-85), the second-order equations for the ECFL Green's function are as follows:

$$\mu(k) = 1 - \lambda\frac{n}{2} + \lambda^2\,\frac{n^2}{4} + \lambda^2\Psi(k), \tag{2}$$

$$\Psi(k) = -\sum_{p,q}(\varepsilon_p + \varepsilon_{k+q-p} + \varepsilon_k + \varepsilon_q + J_{k-p} - u_0) \times \mathbf{g}(p)\,\mathbf{g}(q)\,\mathbf{g}(q+k-p), \tag{3}$$

$$\mathbf{g}^{-1}(k) = i\omega_n + \boldsymbol{\mu}' - \overline{\varepsilon}_k - \lambda^2\,\overline{\Phi}(k), \tag{4}$$

$$\overline{\varepsilon}_k = \left(1 - \lambda\, n + \lambda^2\,\frac{3n^2}{8}\right)\varepsilon_k + \lambda\,\sum_q \tfrac{1}{2} J_{k-q}\,\mathbf{g}(q), \tag{5}$$

$$\overline{\Phi}(k) = -\sum_{q,p}\mathbf{g}(q)\,\mathbf{g}(p)\,\mathbf{g}(k+q-p) \times (\varepsilon_k + \varepsilon_p + \varepsilon_q + \varepsilon_{k+q-p} + J_{k-p} - u_0\,) \times \left\{\varepsilon_k + \varepsilon_p + \varepsilon_q + \varepsilon_{k+q-p} + \tfrac{1}{2}(J_{k-p} + J_{p-q}) - u_0\right\}, \tag{6}$$

where $\sum_k \equiv \frac{1}{\beta N_s}\sum_{\vec{k},\omega_n}$, with N_s being the number of lattice sites and β is inverse temperature. These expressions for the Green's function satisfy the "shift invariances" described in

Ref. 2, i.e., any uniform shift in ε_k or J_k can be absorbed in $\boldsymbol{\mu}'$ and u_0 such that the spectral function is invariant. These second-order equations are the lowest-order ones where nontrivial frequency dependence arises and are the focus of this work. Below we discuss in detail the criterion for the quantitative validity of the present second-order expansion.

As written here, $\mu(k)$ and $\mathbf{g}(k)$ have acquired a variety of static terms as well as frequency-dependent terms called Ψ and $\overline{\Phi}$, respectively. This is written with a slight change of notation $[\Phi(k)]_1 \to \overline{\Phi}(k)$ from (I-85), and we have introduced the effective band energy $\overline{\varepsilon}_k$ in Eq. (5) that gets a static contribution from shrinking of the bare energies ε_k, as well as from the exchange energy J. The role of the parameter u_0 as a second chemical potential is described below. All terms are understood to be correct up to $O(\lambda^2)$, and hence possess corrections of $O(\lambda^3)$ that are ignored here.

The number of the physical electrons is fixed by the number sum rule:

$$\frac{n}{2} = \sum_k \mathcal{G}(k)\, e^{i\omega_n 0^+}. \tag{7}$$

In order for $\mathcal{G}$ to satisfy the Luttinger volume theorem, the auxiliary Fermions described by $\mathbf{g}$ must be equal in number and therefore satisfy a *second* sum rule:

$$\frac{n}{2} = \sum_k \mathbf{g}(k)\, e^{i\omega_n 0^+}. \tag{8}$$

In contrast to canonical theories, here we have two independent sum-rule constraints requiring two Lagrange multipliers. The first Lagrange multiplier $\boldsymbol{\mu}'$ is a standard chemical potential in that it sits next to the band energies $\overline{\varepsilon}_k$ in the denominator of $\mathbf{g}$. A second Lagrange multiplier u_0 arises naturally in the ECFL formalism, thanks to the role of the shift identities, as shown in (I). The u_0 term has a role similar to that of the Hubbard U in the effective Hamiltonian in (I). It controls the broadening of the spectral function through the magnitude of Φ and Ψ. Neither of these Lagrange multipliers is the physical thermodynamic chemical potential of the grand canonical ensemble. The physical chemical potential $\mu_{\rm phys}$, denoted by $\boldsymbol{\mu}$, can be obtained as a function of $\boldsymbol{\mu}'$ and u_0, as shown in Eq. (179) of (I):

$$\begin{aligned}\boldsymbol{\mu} = \boldsymbol{\mu}' &+ u_0 \frac{\lambda n}{2}\left(1 - \frac{\lambda n}{4}\right) \\ &- \left[J_0 \frac{\lambda n}{4}\left(1 - \frac{\lambda n}{2}\right) + 2\lambda\left(1 - \frac{\lambda n}{8}\right)\sum_q \varepsilon_q \mathbf{g}(q)\right] \\ &+ O(\lambda^3).\end{aligned} \tag{9}$$

We now discuss the criterion for validity of equations to a second order in λ. As stated above, dropping terms of $O(\lambda^3)$ in Eqs. (2)–(6) limits the regime of validity of these calculation to densities not too close to unity. To see this, note from Eq. (2) that this theory would give a high-frequency behavior of $\mathcal{G} \sim \frac{c_0}{i\omega}$ with $c_0 = 1 - \frac{n}{2} + \frac{n^2}{4}$, rather than the exact value $c_0 = 1 - \frac{n}{2}$, thus introducing an error. This slight error in the high-frequency physics is a result of keeping a few terms in the expansion in λ. Note, however, that the low-frequency physics encoded by the Luttinger-Ward sum rule is untouched by this and is exactly obeyed to each order in λ. Thus at $n \sim 0.78$ we have an error of $\frac{n^2}{4-2n} \sim 25\%$ in the high-frequency spectral weight in this theory, a value somewhat beyond where we can push this approximation. The $O(\lambda^3)$ terms are expected to extend the range of this approximation to higher particle densities.

III. COMPUTATION OF SPECTRAL FUNCTIONS

A. Definitions

Computationally, it is expedient to employ a spectral function notation as described for example in Ref. 9. The Matsubara frequency object $\mathcal{G}(k, i\omega_n)$ is analytically continued to the real axis and we define as follows:

$$\rho_{\mathcal{G}}(k,\omega) = -\frac{1}{\pi}\mathrm{Im}\,[\mathcal{G}(k, i\omega_n \to \omega + i0^+)]. \tag{10}$$

This object is the spectral function, denoted in most experimental literature by $A(k,\omega)$. The real part of the analytically continued function can be obtained by a Hilbert transform

$$\mathrm{Re}\,\mathcal{G}(k,\omega) = \mathrm{P.V.}\int_{-\infty}^{\infty} \frac{\rho_{\mathcal{G}}(k,\nu)}{\omega - \nu} d\nu. \tag{11}$$

An analogous definition is given for spectral representation $\rho_{\mathbf{g}}(k,\nu)$, $\rho_{\overline{\Phi}}(k,\nu)$, $\rho_{\Psi}(k,\nu)$ used for $\mathbf{g}$, $\overline{\Phi}$, Ψ, etc., and hence, the full set of equations above can be rewritten in terms of these spectral functions. Since $\mathcal{G}$ is a product as in Eq. (1), we note that within the $O(\lambda^2)$ theory

$$\begin{aligned}\rho_{\mathcal{G}}(k,\omega) = \rho_{\mathbf{g}}(k,\omega)&\left(1 - \frac{n}{2} + \frac{n^2}{4} + \mathrm{Re}\,\Psi(k,\omega)\right) \\ &+ \rho_{\Psi}(k,\omega)\,\mathrm{Re}\,\mathbf{g}(k,\omega),\end{aligned} \tag{12}$$

so the two sum rules Eq. (7) and Eq. (8) can be written as

$$\begin{aligned}\frac{n}{2} &= \sum_k \int d\omega \rho_{\mathbf{g}}(k,\omega) f(\omega), \\ \frac{n^2}{4}\left(1 - \frac{n}{2}\right) &= -\sum_k \int d\omega f(\omega)(\rho_{\mathbf{g}}(k,\omega)\,\mathrm{Re}\,\Psi(k,\omega) \\ &\qquad + \mathrm{Re}\,\mathbf{g}(k,\omega)\,\rho_{\Psi}(k,\omega)),\end{aligned} \tag{13}$$

where $f(\omega) = [1 + \exp(\beta\omega)]^{-1}$ and $\overline{f}(\omega) = 1 - f(\omega)$. The auxiliary spectral function is in the usual Dysonian form,

$$\rho_{\mathbf{g}}(k,\omega) = \frac{\rho_{\overline{\Phi}}(k,\omega)}{\{\omega + \boldsymbol{\mu}' - \overline{\varepsilon}_k - \mathrm{Re}\,\overline{\Phi}(k,\omega)\}^2 + (\pi\rho_{\overline{\Phi}})^2}. \tag{14}$$

Using Eqs. (1)–(6), we express the spectral functions for Ψ and $\overline{\Phi}$ as

$$\begin{aligned}\rho_{\overline{\Phi}}(k,\omega) = \frac{1}{N_s^2}\sum_{pq}\int d\nu_1 d\nu_2\, &\rho_{\mathbf{g}}(p,\nu_1)\rho_{\mathbf{g}}(q,\nu_2)\rho_{\mathbf{g}}(p+q-k,\nu_1+\nu_2-\omega) \\ &\times\{f(\nu_1)f(\nu_2)\bar{f}(\nu_1+\nu_2-\omega) + \bar{f}(\nu_1)\bar{f}(\nu_2)f(\nu_1+\nu_2-\omega)\} \\ &\times(\varepsilon_p + \varepsilon_{k+q-p} + \varepsilon_k + \varepsilon_q + J_{k-p} - u_0)\left\{\varepsilon_k + \varepsilon_p + \varepsilon_q + \varepsilon_{k+q-p} + \tfrac{1}{2}(J_{k-p} + J_{k-q}) - u_0\right\},\end{aligned} \tag{15}$$

$$\rho_\Psi(k,\omega) = \frac{1}{N_s^2}\sum_{pq}\int d\nu_1 d\nu_2\ \rho_{\mathbf{g}}(p,\nu_1)\rho_{\mathbf{g}}(q,\nu_2)\rho_{\mathbf{g}}(p+q-k,\nu_1+\nu_2-\omega)$$
$$\times\{f(\nu_1)f(\nu_2)\bar{f}(\nu_1+\nu_2-\omega)+\bar{f}(\nu_1)\bar{f}(\nu_2)f(\nu_1+\nu_2-\omega)\}$$
$$\times(\varepsilon_p+\varepsilon_{k+q-p}+\varepsilon_k+\varepsilon_q+J_{k-p}-u_0). \quad (16)$$

These frequency integrals are solved by discretizing frequency over a finite window that is wide enough to capture the finite support of the spectral functions. In Ref. 27 we outline how this is accomplished efficiently with FFTs and implemented in an iterative process.

IV. RESULTS

A. Physical variables

The computational program has several parameters that can be varied. These include the tight-binding band structure (through hopping parameters t, t' etc.), the spin coupling J, density, and temperature. For the parameters of the model, we focus on a minimal model with the nearest-neighbor hopping $t \sim 3000$ K and $J \sim 900$ K, and all longer-range hopping parameters are zero. These values are chosen to match the bandwidth of the cuprates. However, at the bare level, this produces an electronlike Fermi surface near half filling, remaining closed around the $\Gamma = (0,0)$ point in the Brillouin zone (BZ). This is in contrast to the ARPES reconstructed FS of, say, $BISSCO$ displaying a holelike surface. Nonetheless, this minimal parameter set exhibits a variety of features in common with the cuprates, most notably, a broad incoherent spectrum at high negative frequency. Interestingly, we find that the distribution of incoherent weight at high frequencies is very sensitive to the bare hopping parameters. For this reason, when we look the high-energy features, we will explore their dependence in the second neighbor hopping parameter t', also including a fine-tuned tight-binding fit of $BISSCO$ from Ref. 28.

B. Other parameters in the programs

The program can be implemented on lattices of various size and spatial dimension. For a given choice of these parameters an appropriate choice must be made for computational grid. This includes the lattice size as well as the discretized frequency grid. We look at converged spectral functions for a wide variety of these parameters.

The majority of the following results were performed on a square lattice with dimension $L \times L$ with $L = 36$, and periodic boundary conditions are imposed. We therefore work in a momentum representation with an $L \times L$–sized k grid of points $k_{i,j} = \frac{\pi}{aL}(i,j)$, where $1 \leqslant i,j \leqslant L$ and the lattice parameter is $a = 3.82$ Å. The spectral functions have compact support, extending to $|\omega| \lesssim 8 \times t$. We choose a frequency range $-\frac{1}{2}\omega_c \leqslant \omega \leqslant \frac{1}{2}\omega_c$, with $\omega_c = 30 \times t$, a range that is sufficient to capture the full range of the spectral functions. We discretize this frequency range in $N_\omega = 3000$ bins each of width $\Delta\omega = \frac{\omega_c}{N_\omega} = 0.01t = 30$ K. $\Delta\omega$ is the lowest resolvable frequency scale in the calculation, so it is prudent to disallow any spectral features from becoming any sharper than this scale. Therefore we introduce the convergence factor $\eta_{\min} = \Delta\omega$. It serves as a lower limit on the width of spectral features. Thus in the Dysonian form of $\rho_{\mathbf{g}}$ [Eq. (14)] we set $\rho_{\overline{\Phi}} \rightarrow \rho_{\overline{\Phi}} + \frac{\eta}{\pi}$.

C. Frequency independent variables

We now proceed to study the FS in this theory, starting with the momentum occupation function m_k of the Gutzwiller projected fermions:

$$m_k \equiv \langle \hat{C}^\dagger_{k\sigma}\hat{C}_{k\sigma}\rangle = \int_{-\infty}^{\infty}\rho_{\mathcal{G}}(\vec{k},\omega)f(\omega)d\omega. \quad (17)$$

A sharp drop in this function helps to locate the FS at low T. This can be compared with the Luttinger-Ward surface, defined by a sign change in Re $\mathcal{G}(k,0)$, also given in terms of the spectral function by

$$\text{Re}\ \mathcal{G}(\vec{k},0) = P.V.\int_{-\infty}^{\infty}\frac{\rho_{\mathcal{G}}(\vec{k},\omega)d\omega}{\omega}. \quad (18)$$

At $T = 0$ the FS in $\vec{k}$ space is traced out by Re $\mathcal{G}^{-1}(\vec{k},0) = 0$, as dictated by the Luttinger-Ward sum rule. The momentum distribution m_k is plotted in Fig. 1 at $T = 130$ K and $T = 605$ K for various densities along three principle directions of the BZ. The Luttinger-Ward zero crossings Re $\mathcal{G}^{-1}(\vec{k},0) = 0$ are depicted by dashed vertical lines. There is a close correspondence between these crossings and the point where $m_k = 0.5$, similar to that noted previously by Stephan and Horsch[13] in an exact diagonalization study. Since this correspondence is not on any rigorously firm basis, it is difficult to do more than to list the conditions for its approximate validity. Using high-temperature expansions for the t-J model, Singh and Glenister[14] found the FS to be that of the Fermi gas by various criteria, and noted that the condition $m_{k_F} \sim 0.5$ is only satisfied approximately at high T. At higher temperature where the quasi-particle (QP) near the FS have been significantly broadened, we find that the condition $m_{k_F} \sim 0.5$ is still reliable, in agreement with Ref. 13.

In Fig. 1, a point of considerable interest is the spillover of the occupation to the regions in k space that are unoccupied in the Fermi gas, as noted in various variational wave-function studies of the t-J model already.[15–17] From Eq. (17) we note that the magnitude of m_k for momenta $k > k_F$ provides an estimate of the spectral weight $\rho_{\mathcal{G}}(k,\omega)$ *at occupied energies* at low T. In early analyses of ARPES data, the significance of this piece of information was not always realized, and often substantial spectral weight was discarded as belonging to some unspecified background. Only recent studies such as Ref. 3 have taken note of the significance of the background.

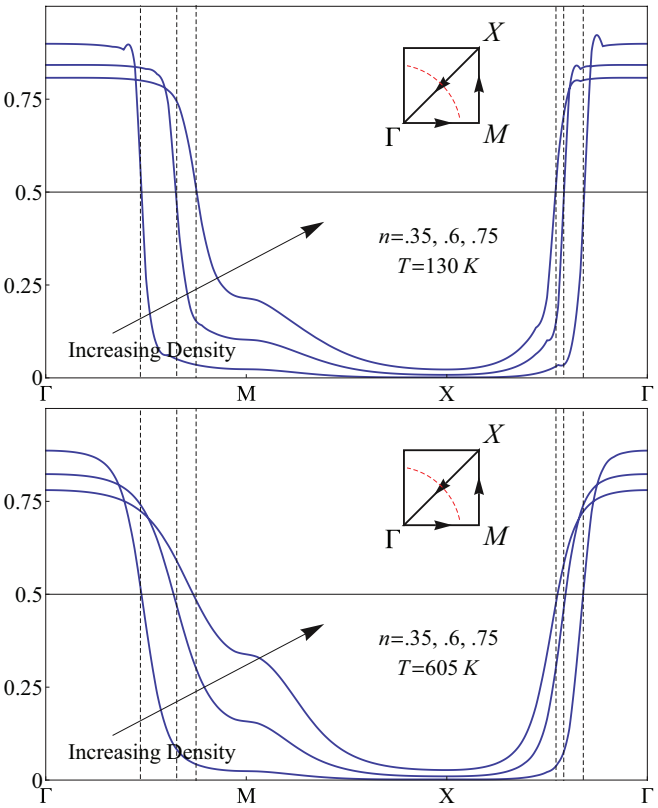

FIG. 1. (Color online) The momentum distribution function m_k is plotted along three principle lines of the BZ. The left and right figures are at 130 and 605 K, respectively. In each case the FS is the same as in the noninteracting problem. The Luttinger-Ward crossing Re $\mathcal{G}^{-1}(\vec{k},0) = 0$ is indicated for each density by the vertical dashed lines. For each density and each temperature the Luttinger-Ward crossings correspond well with the condition $m_k = \frac{1}{2}$.

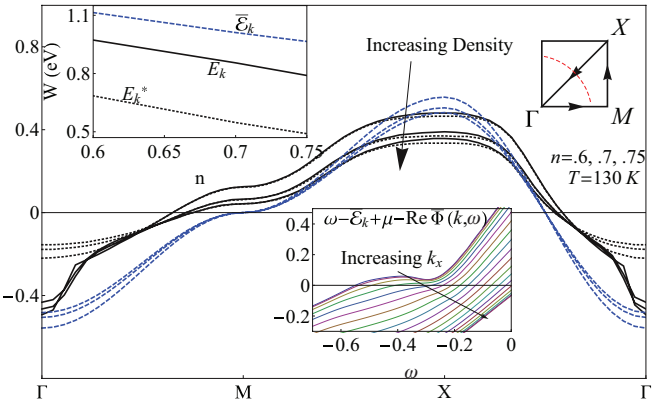

FIG. 2. (Color online) $T = 130$ K. The three dispersions defined in Eq. (19) are plotted along principle directions for three different densities. The upper insets show the bandwidth of the dispersions as a function of the density. The bare bandwidth is 2 eV, but each of these dispersions shrinks compared to that scale. The bandwidth renormalization due to Re $\overline{\Phi}$ in Eq. (19) is k dependent, and so E_k has a different shape than ϵ_k. Note that $E_k \sim E_k^*$ near the FS. However, E_k^* differs from E_k near the Γ point for each of the densities. The lower inset shows the evolution of the real part of the denominator of $\mathbf{g}(k,\omega)$ with ω to illustrate the origin of the difference between E_k and E_k^*. In the inset E_k is determined by the zero crossings of the curves. At low k notice that a relatively flat feature develops with a shallow minimum near $\omega = -0.3$ eV. The minimum corresponds to the peak E_k^*. For increasing k, the flat feature quickly disappears and the zero crossing moves quickly upward in frequency, producing the observed kink in E_k.

D. Various excitation energies

The spectra obtained here contain sharp peaks as well as substantial incoherent background due to extreme correlations. The QP weight Z_k is discussed in the Supplemental Material.[27] To understand the effect of the many-body renormalizations, it is fruitful to study three dispersion relations defined in Ref. 4:

$$\begin{aligned} \overline{\varepsilon}_k &= \left(1 - n + \frac{3n^2}{8}\right)\varepsilon_k + \frac{1}{2}\sum_q J_{k-q}\, m_q, \\ E_k &= \overline{\varepsilon}_k - \boldsymbol{\mu}' + \mathrm{Re}\,\overline{\Phi}(k,E_k), \\ E_k^* &= \max[\rho_{\mathcal{G}}(k,\omega) : \omega]. \end{aligned} \tag{19}$$

Here $\overline{\varepsilon}_k$ defines the bare energy times its static renormalization, while E_k locates the vanishing point for the real part of the auxiliary Green's function $\mathbf{g}$, thereby defining the Luttinger-Ward surface through a change of sign. E_k^* locates the highest peak of the physical Green's function $\mathcal{G}$, and hence defines QP excitations, provided they are sufficiently sharp. ARPES experiments performed with constant k, termed the energy distribution curves (EDCs), locate E_k^* as the peak locations; thus $E_{EDC}(k) \leftrightarrow E_k^*$. On the other hand, the momentum distribution curves (MDCs) are obtained by fixing ω and by scanning k. The so-obtained peak locations yield the fourth dispersion spectrum E_{MDC}. To obtain E_{MDC} in practice, one may invert the MDC peak locations through

$$k^*(\omega) = \max[\rho_{\mathcal{G}}(k,\omega) : k], \quad E_{MDC}(k) = \text{Inverse of } k^*(E). \tag{20}$$

It is worth mentioning that the high-energy kink (or the waterfall) is experimentally defined as the the peeling off of the $E_{MDC}(k)$ from the $E_{EDC}(k) = E_k^*$ spectra.[29]

In Fig. 2 we illustrate the density dependence of the three dispersions in Eq. (19). The inset shows the bandwidths, $W(n)$, of the three dispersions as a function of the density. Note that the bare bandwidth of ϵ_k is 2 eV for both cases. Near the FS we see that $E_k \approx E_k^*$, but they differ near the Γ point where E_k^* and E_{MDC} are also split off from each other, satisfying the above operational definition of the high-energy kink. We now discuss the origin of these splittings.

Although E_k is not directly experimentally relevant, it plays a significant role in the theory, so we first comment on the splitting between E_k and E_k^* near the Γ point. Since E_k is defined as the root of Re $\mathbf{g}^{-1}(k,E_k) = 0$, we plot $\omega + \boldsymbol{\mu}' - \overline{\varepsilon}_k - \mathrm{Re}\,\overline{\Phi}(k,\omega)$ at various k as a function of ω in the inset of Fig. 2. A strong ω dependence of Re $\overline{\Phi}(k,\omega)$ causes a flattening of the curves near the zero crossing between -0.6 and -0.3 eV, and this causes the E_k to fall rapidly with k in the main figure, Fig. 2. Just as E_k breaks away from E_k^*, so also does E_{MDC}, resulting in the kink. This is shown most clearly in the left panel of Fig. 3, where the spectral function is depicted as a color density plot with the dispersions (E_k, E_k^*, E_{MDC}) overlaid. Near the Γ point where $k = (0,0)$ the QP becomes incoherent and the bulk of its spectral weight is

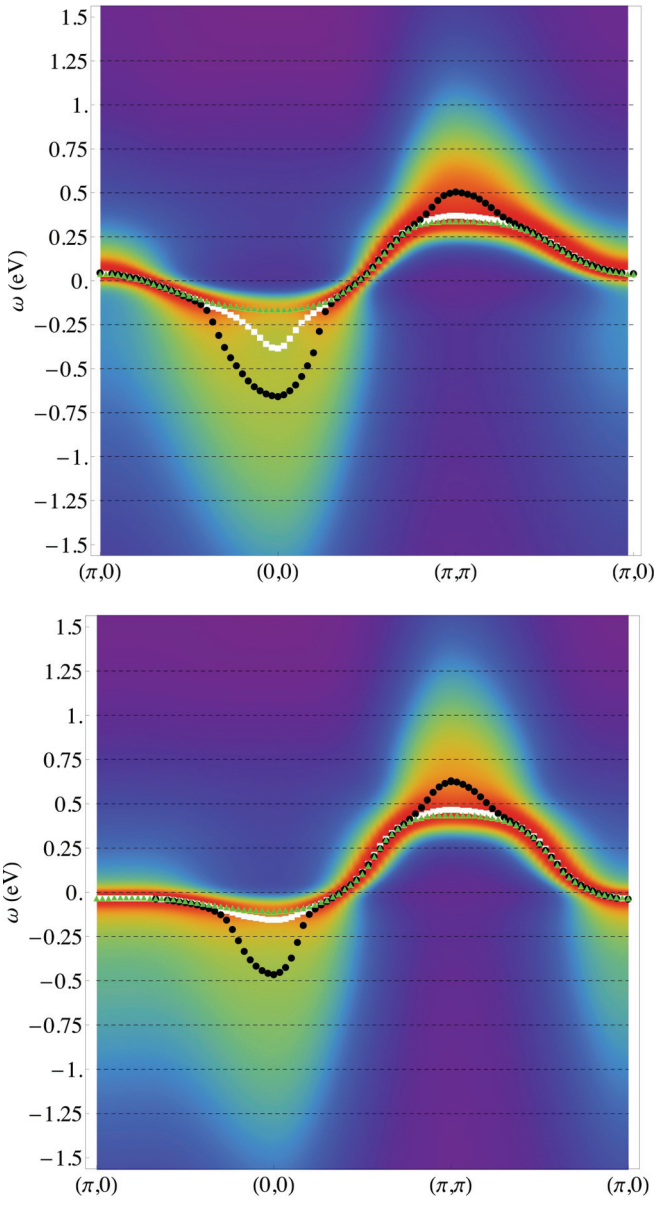

FIG. 3. (Color online) $L = 60$, $(n,T) = (0.75,300)$ K. Density plot of $A(k,\omega)$ of the minimal model (top) and the refined model Ref. 28 (bottom). (Here and below, red denotes high intensity and blue denotes low intensity). E_k, E_k^*, and $E_{MDC}(k)$ spectra are white, green, and black, respectively. Near k_F we see that the three spectra coincide. In the region near $k = (0,0)$, $E_{MDC}(k)$ is at a significantly higher energy scale than E_k or E_k^*, signifying the high-energy kink (waterfall) effect. Also, the EDC peak loses weight in this regime. A new feature arises at near $k = (\pi,\pi)$ resembling an inverted waterfall.

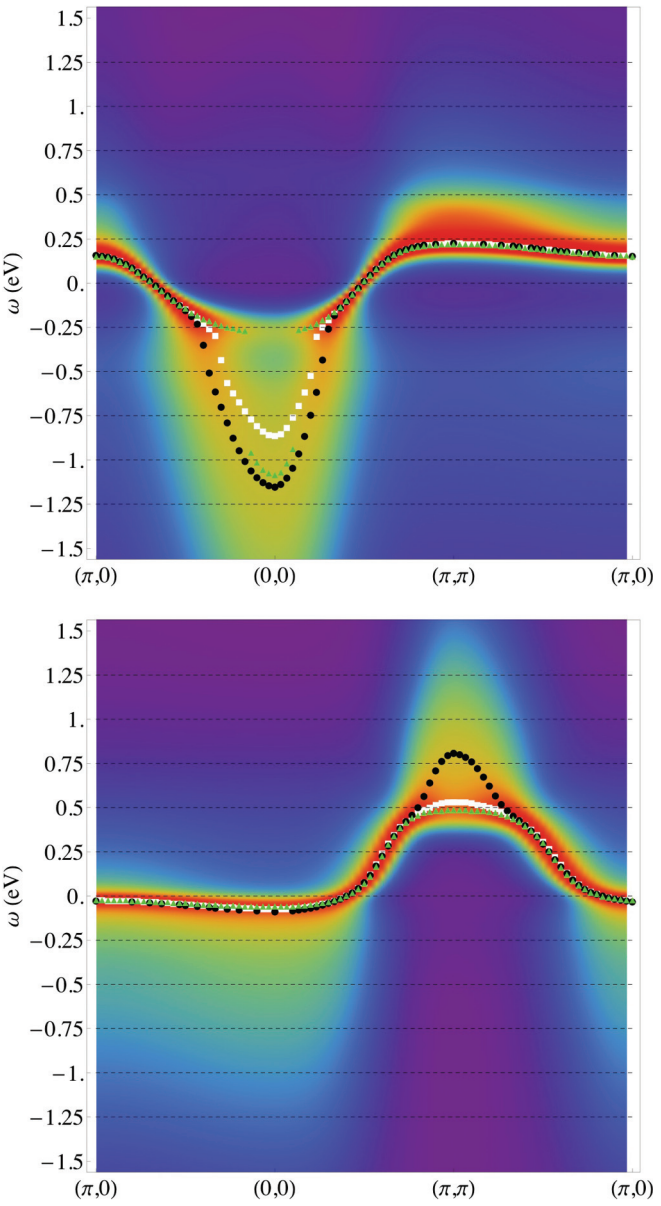

FIG. 4. (Color online) $L = 60$, $(n,T) = (0.75,300)$ K. (Top) $t'/t = 0.4$ is used to model electron-doped high-T_c superconductors. The kink feature is prominent here. (Bottom) Uses $t'/t = -0.4$ to crudely model a holelike FS. In this case the kink near (0,0) is lost, unlike in Fig. 3, correlating with a flat (bare) band dispersion.

spread out to high negative frequencies. In this region E_{MDC} differs considerably from E_k^* and recovers the scale of the bare dispersion ϵ_k. The right panel of Fig. 3 shows the spectral function as calculated using the tight binding parameters of $BISSCO$ given in Ref. 28. These parameters result in a holelike FS around the Γ point, unlike the minimal model with an electronlike FS. However, we observe in Fig. 3 that the high-energy kink occurs for both sets of parameters.

The occurrence of the high-energy kink is understandable as a straightforward consequence of additional broad peaks in the spectral function, separated from the quasiparticle-type peaks. In an energy range where they exist, these are particularly effective in dominating E_{MDC} and less prominent in E_{EDC}, therefore resulting in the separation between these dispersions.

While the qualitative picture of the kinks is reasonably clear, it is not immediately clear what accounts for the slightly different magnitude of the scale of the high-energy kink in Fig. 3. In Fig. 4 we show density plots of the spectral function with $t'/t = \pm 0.4$. The case $t' = 0.4 \times t$ on the left has greater curvature at the band bottom and is identified with the phenomenology of the electron-doped cuprates (Refs. 22,30). The QP peaks lose most of their weight, unlike in the minimal case. The resulting scale of the drop in the waterfall is bigger

than in the minimal case, and correlates well with experimental observations in Ref. 31.

We note in Fig. 4 (right) that the case $t'/t = -0.4$ has no measurable waterfall near the Γ point. The background at negative frequency is essentially featureless, and the QP peaks maintain their spectral weight. However, at positive frequencies, an inverted waterfall-like feature develops near $k = (\pi,\pi)$. This particular parametrization is often invoked to rectify the electronlike curvature of the minimal model ($t' = 0$), but ends up giving a very flat band bottom at Γ. This is unlike the more sophisticated band parameters in Ref. 28, where the curvature is also holelike, and now the band regains significant curvature at its bottom, resulting in the observed kink.

E. Detailed spectral line shapes (EDCs)

In this section, we present detailed line shapes for the spectral function. In an earlier work,[3] we have compared the results of the simplified ECFL formalism. These included some phenomenological inputs, with the experimental data at somewhat higher particle densities $n \sim 0.85$, and found remarkably good agreement with the line shapes. We are content in this work to present the results at lower particle densities, but *from a microscopic calculation* of ECFL. This is made possible by solving the $O(\lambda^2)$ equations in Eq. (6) numerically. The line shapes obtained here have a similar general nature as the ones in Ref. 3, giving support to that work. However, as one expects from a lower-density situation, we find somewhat less dynamical asymmetry about zero energy. More detailed comparison with data near optimal doping with the microscopic ECFL theory must await the solution of the third- or higher-order equations, where the criterion for validity discussed above [see paragraph following Eq. (8)] is satisfied more closely than here.

Let us first examine the local density of states (LDOS) at $n = 0.75$ for both cases at low T in Fig. 5. A prominent feature is that the main peak is much narrower than in the bare LDOS. Furthermore, there is a long tail extending to (negative)

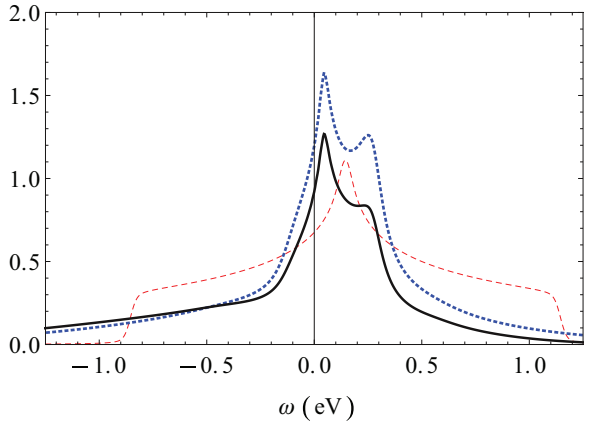

FIG. 5. (Color online) $n = 0.75$. The LDOS of the physical $\mathcal{G}$ (auxiliary $\mathbf{g}$) is in black (dotted blue), and the bare DOS is the dashed red curve. The renormalized band displays narrowing, and a long tail at $\omega < 0$. The LDOS develops a second spectral peak for $\omega > 0$ from a strongly k-dependent feature in the self-energy.

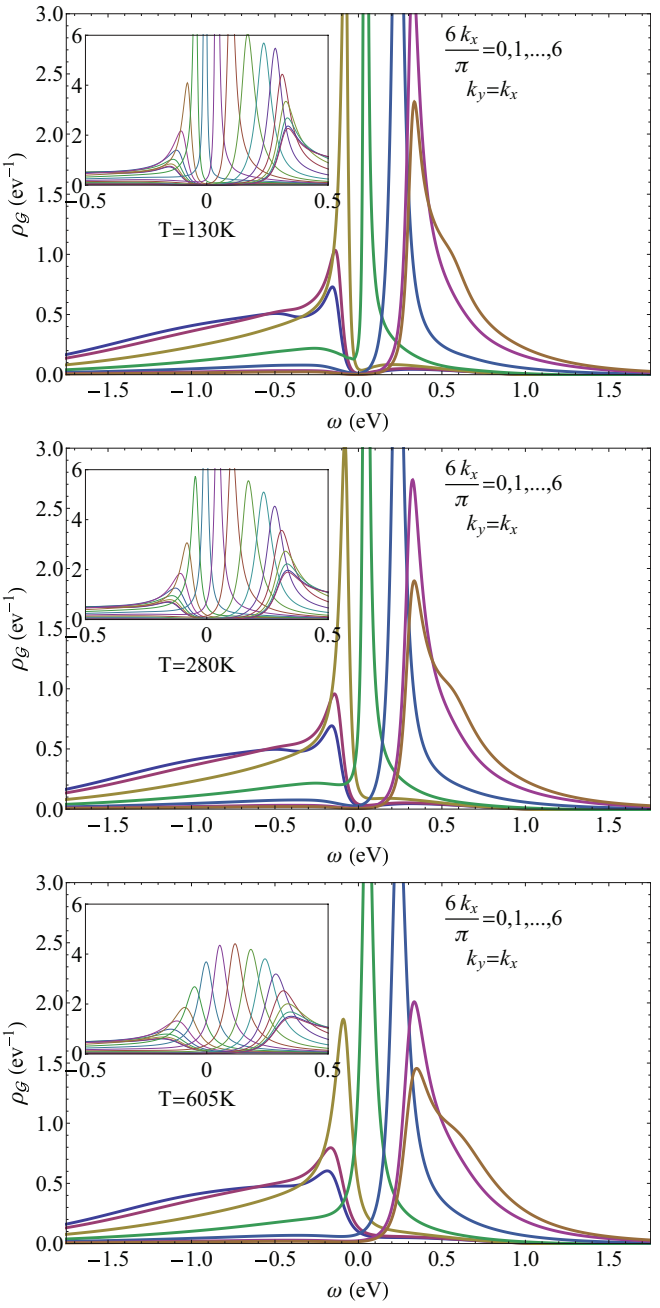

FIG. 6. (Color online) $n = 0.75$. The spectral function $\rho_{\mathcal{G}}$ [$= A(k,\omega)$] at several k points along the $\langle 11\rangle$ direction and T. We used $L_x = 36$; the insets show all positive k_x's and the main figures display a third of the allowed k_x's. The inset in each case zooms out to reveal the heights. The linewidth near k_F is seen to be strongly effected by rising T; the incoherent parts have very little T dependence. The tails exhibit a secondary broad peak near $\omega = -0.4$ eV, giving rise to the high-energy kink (waterfall).

frequencies, much greater than those seen in the bare LDOS. Finally, we note that the LDOS acquires a second peak at positive frequency. This peak arises due to some k-dependent features in the self-energy (discussed below), resulting in sharper QP at positive frequency.

We next discuss Fig. 6, displaying the nodal spectral function at three different temperatures. The lines are quite

sharp near k_F but broaden out rapidly away from k_F. The insets give an idea of the change of spectral density with temperature. Notably, there is a secondary local maximum for k near the Γ point near $\omega = -0.4$ eV. This second peak is responsible for the waterfall discussed above and is also contained in the models used in Refs. 3,5. As discussed above in connection with kinks, its microscopic origin is sensitive to tight binding parameters. It is also noteworthy that lines with $k > k_F$, though broader than at k_F, are sharper than those with $k < k_F$.

Finally, we note that while the self-energy is strongly k dependent it is not anisotropic. Consequently, the EDC line shapes look similar at different parts of the FS, at least to $O(\lambda^2)$. In the regime of validity of this theory, namely, the (hole) overdoped region, the cuprates do not display a strong anisotropy either.

F. Optical conductivity

The optical conductivity $\sigma(\Omega)$ is computed within the lowest approximation of (I) here by discarding the vertex corrections and working with the auxiliary **g**:

$$\mathrm{Re}\sigma(\Omega) = \frac{1}{\Omega}\sum_k v_k^2 \int \rho_{\mathbf{g}}(k,\omega)\rho_{\mathbf{g}}(k,\Omega+\omega)\, d\omega \times [f(\omega) - f(\Omega+\omega)]. \quad (21)$$

The imaginary part of the conductivity can be obtained by a Hilbert transform of the real part. In this purely t-J calculation we must be careful how we interpret the imaginary part of σ. A more realistic calculation should include contributions from the upper Hubbard band and from charge-transfer processes that are significant at high frequencies; these are discarded in the t-J model. For our current purposes we will discuss two kinds of relaxation rates. First we compute a momentum-averaged rate $1/\tau_\sigma$ extracted from the low-frequency behavior $\sigma(\omega)$ using

$$\frac{1}{\tau_\sigma} = \frac{4}{\pi}\int_0^{1/\tau_\sigma} \mathrm{Re}\,\sigma(\omega)/\sigma(0) d\omega, \quad (22)$$

where the prefactor is chosen to yield the usual rate for a Lorentzian shape. This convenient definition is designed to be insensitive to the shape of $\sigma(\omega)$. Secondly, we look at the momentum-resolved scattering lifetimes, defined as the inverse width of the ARPES line shape at the Fermi momentum. These scattering rates are displayed in Fig. 7. We find that the $1/\tau$ curves from ARPES and the conductivity have essentially the same temperature dependence, apart from a factor of $O(1)$. The $1/\tau$ rises quadratically at low temperature, in accordance with the standard Fermi liquid (FL) picture, crossing over to a linear dependence at a fairly low-temperature scale.

In Fig. 8, we display the computed optical conductivity Re $\sigma(\omega)$ at various T for $n = 0.75$, and also the phase angle $\theta = \tan^{-1}(\frac{\sigma''(\omega)}{\sigma'(\omega)})$ on an absolute scale. The rapid fall of the optical conductivity at low T is rapidly filled in at low ω, and the phase angle falls off with ω at about 4000 cm^{-1}. At optimum doping, the phase angle is known experimentally to be flat in ω over a much larger range,[32] and differs from the present calculation, whose validity is confined to overdoping. Experimental measurements in the overdoped case of the phase

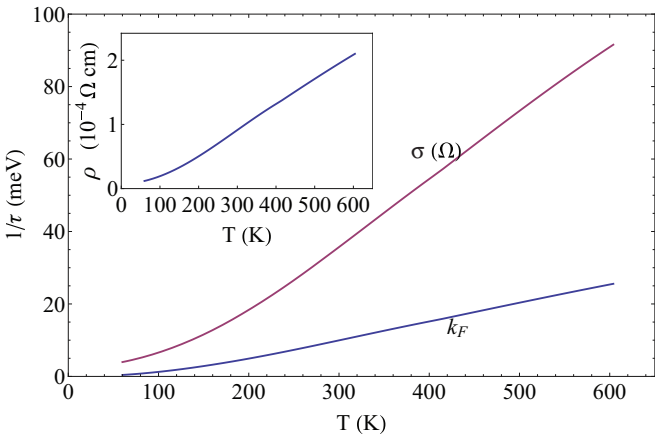

FIG. 7. (Color online) $n = 0.75$. The QP relaxation rate at the FS along $\langle 11\rangle$ obtained from $\rho_\Sigma(k, E_k^*)$, and the rate obtained from the optical conductivity as in Eq. (22). The T^2 behavior of an FL is visible at low temperature, crossing over at a modest temperature ($\sim$150) K, partly due to the shrinking bandwidth, as seen directly in Fig. 2. The inset shows the dc resistivity obtained from the inverse of Eq. (21). It similarly displays a T^2 behavior crossing over to a linear behavior, as well as a lack of saturation that persists to higher T than shown.

angle would be useful in benchmarking theories in regimes such as the present one. For the real part, such a comparison is possible. In Fig. 9 we display the Re $\sigma(\omega)$ curves along with optical conductivity measurements published by Puchkov *et al.*[12] for an overdoped thallium compound. We note that in the overdoped regime, the computed conductivity matches quite well with experiments (to within a factor 2 on the vertical scale).

A further interesting aspect of the resistivity obtained from this ECFL formalism lies in the high-temperature limit. A lack of resistivity saturation has been observed in numerical treatments of strongly coupled models, as in a recent DMFT work.[25] These results are in qualitative agreement with resistivity measurements in the cuprates and other strongly

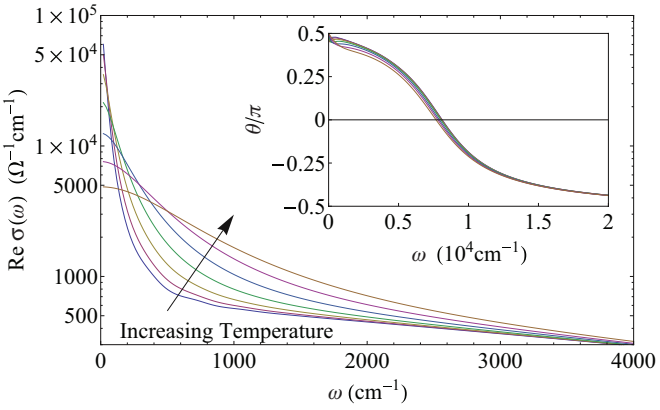

FIG. 8. (Color online) $n = 0.75$, $T = 60,90,130,190,280,410,605$ K. The optical conductivity is calculated on an absolute scale and illustrates how increasing T rapidly fills up the regime $200 \leqslant \omega \leqslant 1000$ cm^{-1}. The rise of conductivity at very low ω is also inferred from the dc resistivity displayed in Fig. 7. The phase of the complex σ falls off rapidly beyond 4000 cm^{-1}.

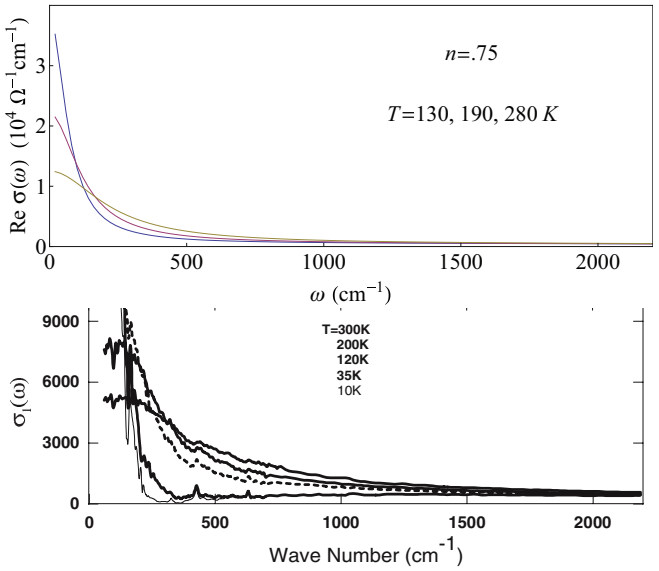

FIG. 9. (Color online) An explicit comparison of optical conductivity with measurements of Puchkov *et al.* from Ref. 12 with the author's kind permission. The data pertains to an overdoped thallium-based cuprate with $T_c = 23$ K, with a density $n \approx 0.75$. We note the similarity of magnitude and variation with ω and T. It is worth noting (to be reported elsewhere) that the vertical scale can be brought into better agreement with an adjusted hopping, as with the Fermi velocity.

correlated compounds. The ECFL theory leads to a similar result and provides a simple picture for its origin in terms of the second Lagrange multiplier u_0. As discussed in the Supplemental Material,[27] both $\boldsymbol{\mu}'$ and u_0 rise linearly with T at high temperature. Due to the explicit appearance of u_0 in the expressions for Φ and Ψ, *the magnitude of the self-energies* also grows continuously with temperature via u_0, resulting in a monotonic broadening of the spectral function. This broadening is insensitive to the Mott-Ioffe-Regel (MIR) saturation expected in weakly correlated metals, and leads to a nonsaturating resistivity at high T, as we observe in the inset of Fig. 7.

G. Self-energies

We now display the self-energies that are involved in calculating the spectral functions. In Fig. 10 we display $\rho_{\overline{\Phi}}$ and ρ_Ψ. Both functions exhibit the ω^2 behavior close to zero, as one finds for a weakly interacting FL self-energy. Unlike conventional FLs, the magnitude of the quadratic term is strongly k dependent. From these functions and the associated real parts we can construct a Dyson-Mori (D-M) self-energy, defined through the equation

$$\mathcal{G} = \frac{a_\mathcal{G}}{x - \Sigma}, \tag{23}$$

where $a_\mathcal{G}$ is the total spectral weight of the physical $\mathcal{G}$ and $x = \omega + \boldsymbol{\mu}' - \overline{\varepsilon}_k$ such that

$$\Sigma = x + \frac{a_\mathcal{G}}{a_\mathcal{G} + \Psi}(\overline{\Phi} - x). \tag{24}$$

In Fig. 11 we plot the computed imaginary part of the D-M self-energy, ρ_Σ. It exhibits a similar magnitude and k dependence at

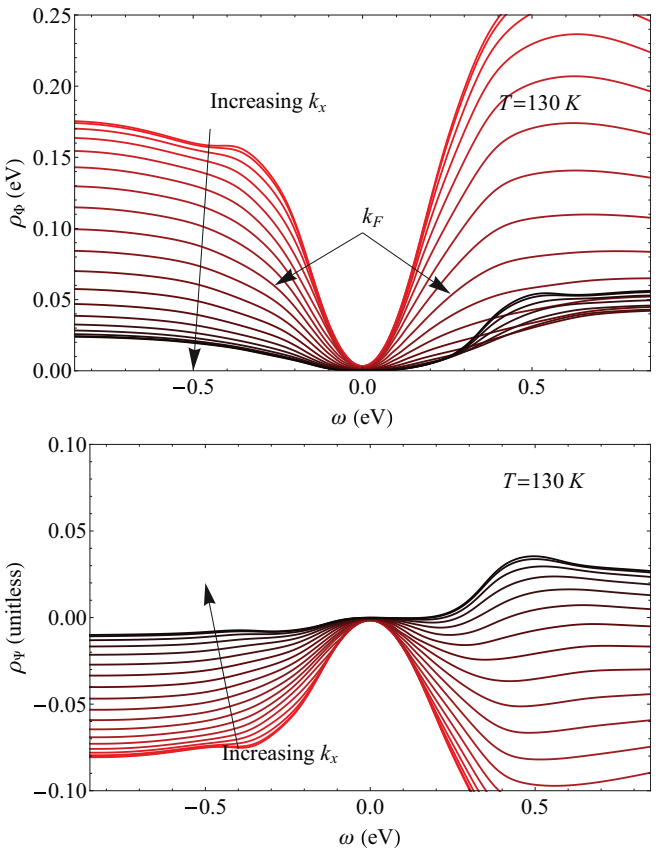

FIG. 10. (Color online) $(n,T) = (0.75,130)$ K. The spectral functions for the two self-energies Φ and Ψ, i.e., $\rho_{\overline{\Phi}}$ (top) and ρ_Ψ (bottom), at several k points along the $\langle 11 \rangle$ direction. Both are roughly quadratic and symmetric at low frequency but have a strongly k-dependent curvature. In the plot of $\rho_{\overline{\Phi}}$, the minimum width η chops off the bottom of the low-frequency minimum.

low frequency to that in $\rho_{\overline{\Phi}}$. However, large asymmetries begin to appear at intermediate frequencies. It is interesting that at positive frequency the function is considerably smaller than at negative frequencies, a feature that has already been noted for simplified versions of the ECFL[4,5] and also in a recent DMFT study of the Hubbard model.[25] In this calculation, however, we see an interplay between the momentum and frequency dependencies. In particular, we see that at positive frequency $0 < \omega \lesssim 200$ meV, ρ_Σ is strongly k dependent, so that particlelike excitations near $k = (\pi,\pi)$ are long-lived while those inside the FS suffer a large damping. This is very different from weakly coupled or local theories such as DMFT, where the scattering rate is determined by *frequency alone*. We note that this self-energy does not differentiate between nodal and antinodal directions, but rather, the k dependence arises only through $\varepsilon_{\vec{k}}$, so that the scattering rate is constant along the FS.

The low-frequency asymmetry is usefully described as an FL-like quadratic dependence modified by a cubic term. The right panel of Fig. 11 shows low-frequency ($|\omega| \leqslant 75$ meV) fit parameters of ρ_Σ as a function of k, exhibiting a marked softening of the quadratic coefficient b. The final effect on the relaxation rate $\Gamma(k) = \rho_\Sigma(k, E_k^*)$, displayed in Fig. 12, is

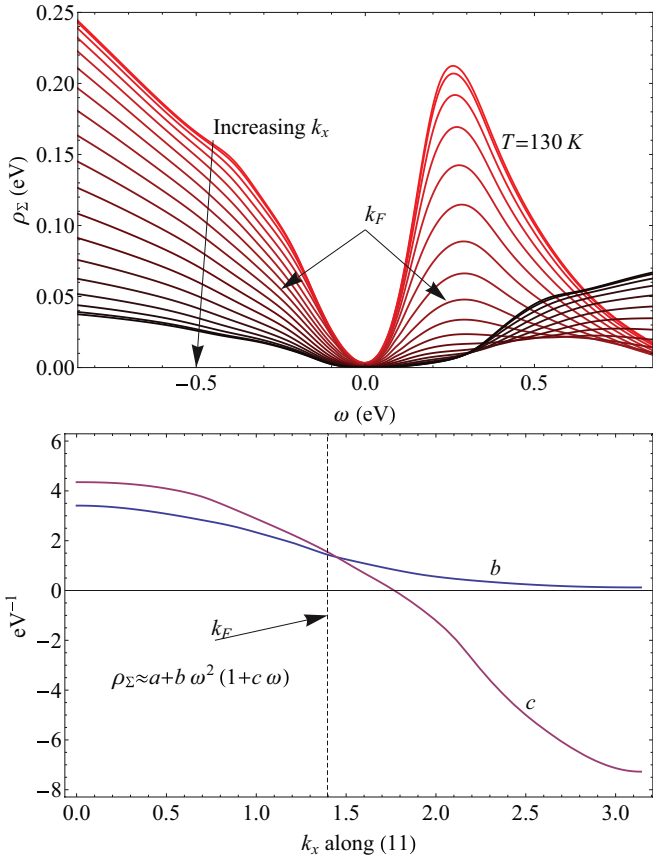

FIG. 11. (Color online) $(n,T) = (0.75,130)$ K. (Top) The spectral function ρ_Σ of the Dyson-Mori self-energy Σ from Eq. (24), at several k points along the $\langle 11 \rangle$ direction. As with $\rho_{\overline{\Phi}}$, ρ_Σ has inherited a strong k dependence. (Bottom) k dependence of the fit parameters from $\rho_\Sigma = a + b\,\omega^2(1 + c\,\omega)$ at low frequencies $|\omega| \leqslant 75$meV. Observe the softening of the quadratic coefficient with increased k. The cubic term $\rho_\Sigma \propto \omega^3$ produces particle-hole asymmetry, as argued in Ref. 6, and grows in magnitude with increasing k beyond k_F.

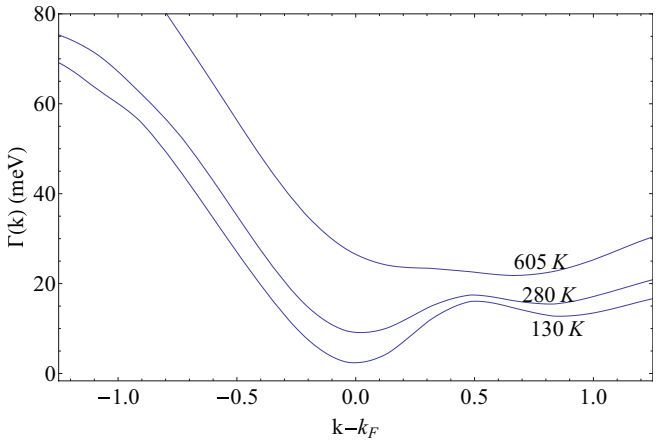

FIG. 12. (Color online) $n = 0.75$. The decay rate of QP near k_F along the nodal line from $\Gamma_k = \rho_\Sigma(k, E_k^*)$. The strong and T-dependent asymmetry makes quasiparticles longer lived at $k > k_F$. With increased T the minimum of Γ moves to $k > k_F$.

summarized by the expression

$$\Gamma(k) \sim b_f \left(1 - \left|\frac{b'_f}{b_f}\right| (k - k_F)\right) V_F^2\,(k - k_F)^2, \qquad (25)$$

where b_f (b'_f) is the coefficient (derivative of the coefficient) at the Fermi momentum, and V_F is the Fermi velocity. The cubic term in $k - k_F$ is a significant correction to the leading term from Fermi liquid theory, resulting in longer-lived quasiparticles outside the Fermi surface, as compared to quasiholes inside the Fermi surface. Furthermore, the T dependence of Γ is stronger at $k < k_F$. At the highest temperature shown, the longest lived quasiparticles drift somewhat away from k_F. In Fig. 7, we also display the T dependence of the single-particle relaxation rate $\Gamma(k)$. This rate shows a crossover at a reduced scale to linear in T behavior, about $\sim$150 K, as compared to $T_{\mu'} \sim 400$ K, detailed in the Supplemental Material.[27]

V. CONCLUDING REMARKS

In summary, we have presented the results of a systematic low-density expansion for the t-J model using the recently developed formalism of *extremely correlated Fermi liquids*, discussed in Refs. 1 and 2. This calculation complements the phenomenological theory in Ref. 3, where the line shapes at optimal doping are successfully modeled, using a very small number of parameters. Here we calculate from first principles, assuming only the value of J and the hopping t, and where possible, quote results on an absolute scale. The second order in λ equations studied here, valid for $n \lesssim 0.75$, are somewhat removed from the most interesting regime of optimal doping. Nevertheless, the computed forms of the twin self-energies found here indeed have the character assumed in the phenomenological ECFL studies; also, the resulting spectral functions have line shapes that are skewed towards negative ω. This feature is ultimately a consequence of Gutzwiller projection, as argued in Ref. 1, and captures a striking characteristic of the experimental data.

The salient points from our study may be summarized as follows:

(i) The momentum occupation function $m_k = \langle \hat{C}_k^\dagger \hat{C}_k \rangle$ is calculated along the nodal direction at various T and densities, where it indicates a large spillover for $k > k_F$. This spillover quantifies the smooth part of spectral weight at $\omega < 0$ for wave vectors $k > k_F$ and is of potential use in calibrating ARPES studies.

(ii) The spectral functions $A(k,\omega)$ at various k values and different temperatures displays a non-Lorentzian form, with a pronounced skew towards occupied energies $\omega < 0$. This results in spectra resembling those seen in most experiments in cuprates and emerges as a natural consequence of the Gutzwiller projection, i.e., very strong correlations.

(iii) The dispersion relations $E_{MDC}(k)$ and $E_{EDC}(k)$ are deduced from the peaks of $A(k,\omega)$ and display considerable band narrowing due to correlations. They further split apart near $\vec{k} \sim (0,0)$, i.e., the Γ point, resulting in a high-energy kink, quite similar to that seen in experiments. The splitting between these peaks is due to a prominent broad second maximum in the spectral function, away from the quasiparticle peak. A high sensitivity of the high-energy kink to the

bare band parameters is found, with flatband dispersions eliminating the kinks.

(iv) The ECFL results for the optical conductivity and the phase angle are reported on an absolute scale, and the real part is in quite reasonable proximity of experimental data. Better agreement should be possible with tuning the available band parameters, although we have not explored this here.

(v) The resistivity is calculated as a function of T at various densities and found to be nonsaturating in its T dependence, analogous to the resistivity seen in experiments. The absence of saturation is easy to understand within the ECFL formalism. The magnitude of the self-energy grows indefinitely due to its dependence on the second chemical potential u_0 and leads to a growing resistivity from the Kubo formula.

(vi) The single-particle decay rate $\Gamma(k,T)$ is reported at various k and T. It is smaller for $k > k_F$ than for $k < k_F$ due to a strong correction to Fermi liquid behavior, leading to spectral lines that are narrower than for $k < k_F$.

ACKNOWLEDGMENTS

This work was supported by the DOE under Grant No. FG02-06ER46319. We thank Gey-Hong Gweon for stimulating discussions and Ehsan Khatami for helpful comments on the manuscript.

[1] B. S. Shastry, Phys. Rev. Lett. **107**, 056403 (2011).
[2] B. S. Shastry, Phys. Rev. B **87**, 125124 (2013).
[3] G.-H. Gweon, B. S. Shastry, and G. D. Gu, Phys. Rev. Lett. **107**, 056404 (2011).
[4] K. Matsuyama and G.-H. Gweon, arXiv:1212.0299.
[5] B. S. Shastry, Phys. Rev. B **84**, 165112 (2011).
[6] B. S. Shastry, Phys. Rev. Lett. **109**, 067004 (2012).
[7] P. Nozières, *Theory of Interacting Fermi Systems* (W. A. Benjamin, Amsterdam, 1964).
[8] A. A. Abrikosov, L. Gorkov, and I. Dzyaloshinski, *Methods of Quantum Field Theory in Statistical Physics* (Prentice-Hall, Englewood Cliffs, NJ, 1963).
[9] G. D. Mahan, *Many-Particle Physics* (Plenum Press, New York, 1981).
[10] M. Bejas, A. Greco, and A. Foussats, Phys. Rev. B **73**, 245104 (2006); E. Cappelluti and R. Zeyher, *ibid.* **59**, 6475 (1999).
[11] A. Pasupathy, A. Pushp, K. Gomes, C. Parker, J. Wen, Z. Xu, G. Gu, Y. Ando, and A. Yazdani, Science **320**, 196 (2008), see especially Figs. 1 A, 1B, and 4A.
[12] A. V. Puchkov, D. Basov, and T. Timusk, J. Phys.: Condens. Matter **8**, 10049 (1996).
[13] W. Stephan and P. Horsch, Phys. Rev. Lett. **66**, 2258 (1991).
[14] R. R. P. Singh and R. L. Glenister, Phys. Rev. B **46**, 14313 (1992).
[15] C. Gros, R. Joynt, and T. M. Rice, Phys. Rev. B **36**, 381 (1987).
[16] B. Edegger, V. N. Muthukumar, and C. Gros, Adv. Phys. **56**, 927 (2007).
[17] A. Paramekanti, M. Randeria, and N. Trivedi, Phys. Rev. Lett. **87**, 217002 (2001).
[18] M. M. Zemljic and P. Prelovsek, Phys. Rev. B **72**, 075108 (2005).
[19] M. M. Zemljic, P. Prelovsek, and T. Tohyama, Phys. Rev. B **76**, 012502 (2007); Phys. Rev. Lett. **100**, 036402 (2008).
[20] J. Kokalj and P. Prelovsek, Phys. Rev. B **75**, 045111 (2007).
[21] J. Jaklic and P. Prelovsek, Adv. Phys. **49**, 1 (2000).
[22] B. Moritz, F. Schmitt, W. Meevasana, S. Johnston, E. M. Motoyama, M. Greven, D. H. Lu, C. Kim, R. T. Scalettar, Z.-X. Shen, and T. P. Devereaux, New J. Phys. **11**, 093020 (2009).
[23] W. Metzner and D. Vollhardt, Phys. Rev. Lett. **62**, 324 (1989).
[24] A. Georges, G. Kotliar, W. Krauth, and M. J. Rozenberg, Rev. Mod. Phys. **68**, 13 (1996).
[25] X. Deng, J. Mravlje, R. Žitko, M. Ferrero, G. Kotliar, and A. Georges, Phys. Rev. Lett. **100**, 086401 (2013).
[26] E. Khatami, D. Hansen, E. Perepelitsky, M. Rigol, and B. S. Shastry, Phys. Rev. B **87**, 161120(R) (2013).
[27] See Supplemental Material at http://link.aps.org/supplemental/10.1103/PhysRevB.87.245101 for details of the results for thermodynamics and the wave-function renormalization Z_k, and further details of the computational method employed.
[28] R. S. Markiewicz, S. Sahrakorpi, M. Lindroos, H. Lin, and A. Bansil, Phys. Rev. B **72**, 054519 (2005).
[29] J. Graf, G.-H. Gweon, K. McElroy, S. Y. Zhou, C. Jozwiak, E. Rotenberg, A. Bill, T. Sasagawa, H. Eisaki, S. Uchida, H. Takagi, D.-H. Lee, and A. Lanzara, Phys. Rev. Lett. **98**, 067004 (2007); W. Meevasana *et al.*, Phys. Rev. B **75**, 174506 (2007).
[30] L. Hozoi, M. S. Laad, and P. Fulde, Phys. Rev. B **78**, 165107 (2008).
[31] S. R. Park, D. J. Song, C. S. Leem, C. Kim, C. Kim, B. J. Kim, and H. Eisaki, Phys. Rev. Lett. **101**, 117006 (2008).
[32] D. van der Marel, H. J. A. Molegraaf, J. Zaanen, Z. Nussinov, F. Carbone, A. Damascelli, H. Eisaki, M. Greven, P. H. Kes, and M. Li, Nature (London) **425**, 271 (2003).

Extremely Correlated Fermi Liquids: Self consistent solution of the second order theory. Supplementary Material

Daniel Hansen and B. Sriram Shastry[1]

[1] *Physics Department, University of California, Santa Cruz, CA 95064, USA*

(Dated: May 10, 2013)

THERMODYNAMICS

In Fig. (13) we display the density dependence of the two Lagrange multipliers, $\boldsymbol{\mu}'$ and u_0, as well as the physical chemical potential, $\boldsymbol{\mu}$, as defined in Eq. (9) of the main paper. The plot illustrates a few points regarding the nature of $\mathbf{g}$ and $\mathcal{G}$, and their differences. First, we see that $\boldsymbol{\mu} \approx \boldsymbol{\mu}'$ in the low density limit. With increased density, u_0 grows monotonically causing the development of large asymmetric tails in the spectral background. Furthermore, with the growth of both density and u_0, $\boldsymbol{\mu}$ grows faster than $\boldsymbol{\mu}'$. While $\boldsymbol{\mu}'$ approaches 0, a limit expected for a half-filled FL with particle-hole symmetry, $\boldsymbol{\mu}$ approaches a limit which is comparable to the renormalized bandwidth, i.e. the top of the band. This difference therefore also signals the reduction of spectral weight in $\mathcal{G}$ relative to $\mathbf{g}$, a symptom of the main constraint of this theory, namely the removal of states with double occupancy.

The temperature dependence of $(\boldsymbol{\mu}', \boldsymbol{\mu}, u_0)$ is shown below in Fig. (14) revealing the temperature scale for the thermodynamics of the ECFL at a single density ($n = .75$). At the lowest temperatures we expect that the chemical potential goes as $\boldsymbol{\mu}'(T) = \boldsymbol{\mu}'(0) - bT^2$ (to focus on the quadratic term we subtract off the $T = 0$ intercepts in Fig. (14)). We can define a temperature scale $T_{\boldsymbol{\mu}'}$ which sets the strength of the $O(T^2)$ term according to

$$T_{\boldsymbol{\mu}'} = \sqrt{\left|\frac{\boldsymbol{\mu}'(0)}{b}\right|}. \tag{S.1}$$

where we have used the auxiliary "chemical potential" $\boldsymbol{\mu}'$ because it is most closely related to the FL aspects of the spectral function. $T_{\boldsymbol{\mu}'}$ is plotted in the inset as a function of the density n. Note the reduction of the scale of $T_{\boldsymbol{\mu}'}$ as we approach half filling. At high T ($> 600K$), $\boldsymbol{\mu}'$ rises linearly with T in typical FL fashion.

We also observe in Fig. (14) that the temperature dependence of $\boldsymbol{\mu}$ comes from $\boldsymbol{\mu}'$ as well as that of u_0 and hence, unlike in a simple FL, is substantially driven by many body effects even at low T. Furthermore, the scale of the temperature variation is larger than would be expected for weakly coupled systems. We note the large variation of the chemical potential with temperature, $\Delta\boldsymbol{\mu} \sim 20meV$ on heating from 100K to 300K, and about half this number for the change for $\Delta\boldsymbol{\mu}'$. This large variation should be readily measurable in ARPES, and appears to have been overlooked in most studies so far.

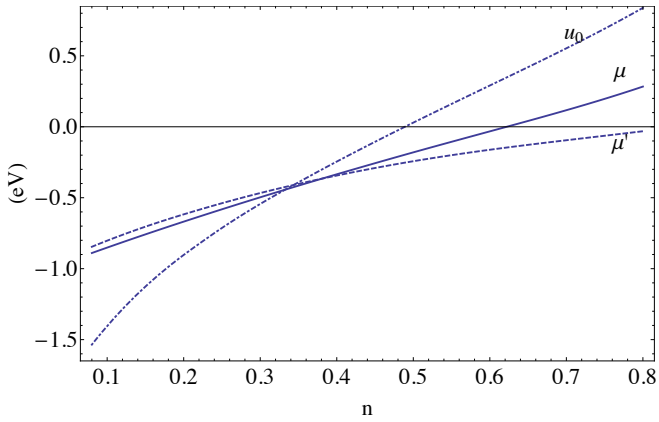

FIG. 13. $T = 280K$. The density dependence of the various chemical potentials, as defined in Eq. (9) of the main paper. The potentials $\boldsymbol{\mu}'$ and u_0, and the net physical chemical potential $\boldsymbol{\mu}$, dashed,dot-dashed, and solid, respectively. The potential $\boldsymbol{\mu}'$ approaches 0 as $n \to 1$, i.e. half filling, while the potential u_0 rises monotonically with density. The physical chemical potential $\boldsymbol{\mu}$ becomes positive at high densities. This is natural for a state where spectral weight has been removed by the single occupancy constraint, so that n=1 corresponds to a filled rather than half-filled band. The scale of $\boldsymbol{\mu}$ and u_0 corresponds to the scale of the renormalized bandwidth in the high density limit.

Unlike $\boldsymbol{\mu}'$, u_0 does not follow the standard behavior of a FL chemical potential. Whereas the low T temperature dependence of $\boldsymbol{\mu}'$ arises from small changes in occupation at low frequency only, u_0 feels *all frequencies* due to its explicit appearance in $\overline{\Phi}$ and Ψ. The scaling with T is therefore difficult to predict by a Sommerfeld type argument. Numerically, we observe linear-T behavior at low T and at high T separated by a minima at an intermediate T. u_0 asymptotes to a T linear behavior for $T \gtrsim 650K$.

QUASIPARTICLE WEIGHT

The spectra obtained here contain sharp peaks, and also substantial background due to extreme correlations which can be quantified after some care is taken in defining a suitable Z_k. In a conventional FL the QP weight is defined by $Z_k = \frac{1}{1-\frac{\partial\Sigma}{\partial\omega}}/_{(k_F,0)}$ where Σ is the Dyson self energy. This definition does not immediately work for us as we do not have a conventional Dysonian form

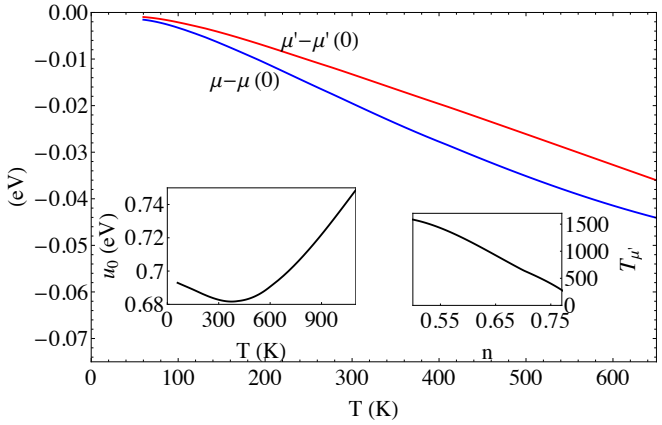

FIG. 14. $\boldsymbol{\mu}'$ and $\boldsymbol{\mu}$ versus T at $n = .75$. An effective Fermi temperature $T_{\mu'}$, found from Eq. (S.1), is shown as a function of the density. Note that the scale of variation of the $\boldsymbol{\mu}'$, $\Delta\boldsymbol{\mu}' \sim 10$ meV in heating from $T = 100$K to $T = 300$K, is quite large and is potentially observable in ARPES. A shrunken overall energy scale, seen most clearly in the reduction of the QP bandwidth, is ultimately responsible for this sensitivity. The temperature dependence of u_0 is shown in each case to be non-monotonic with a minimum at finite temperature. At high temperature u_0 rises linearly with T, similarly to $\boldsymbol{\mu}'$.

for our $\mathcal{G}$. To obtain an appropriate definition for Z_k we note that the ECFL Greens function can be written in a Dyson-Mori form

$$\mathcal{G} = \frac{a_{\mathcal{G}} + \Psi}{x - \overline{\Phi}} = \frac{a_{\mathcal{G}}}{x - \Sigma_{DM}} \tag{S.2}$$

where $a_{\mathcal{G}} = 1 - \frac{n}{2}$ exactly and $x = i\omega + \boldsymbol{\mu} - \bar{\epsilon}_k$. However in the present approximation $a_{\mathcal{G}} = 1 - \frac{n}{2} + \frac{n^2}{4}$ owing to the second order in λ approximation. In analogy to the standard FL we now define

$$Z_k = \frac{a_{\mathcal{G}}}{1 - \frac{\partial}{\partial\omega}\Sigma_{DM}}. \tag{S.3}$$

While it may be tempting to drop the factor $a_{\mathcal{G}}$ from Eq. (S.3), it represents an important piece of physics in the larger context and therefore must be retained. To elaborate this, note that the full spectral function of canonical electrons, e.g. in a large U Hubbard model, would have features at the scale of U that correspond to the upper Hubbard band, and are thrown out in the t-J model thereby isolating the lower Hubbard band. Thus in a comprehensive canonical theory, the (low) value of Z_k representing a faint QP feature found with the present definition, would be compensated by a large background piece with net weight $1 - Z_k$ contained partly in the lower Hubbard band, and partly in the upper Hubbard band that lies outside the domain of the t-J model. It is therefore Eq. (S.3) that can be compared to the values found in experiments, and also in studies of the Hubbard model with large U.

Alternatively, if we define the Dyson self energy according to $\mathcal{G} = \frac{1}{x - \Sigma'}$, the quasiparticle weight would once again be given by the more familiar expression $Z'_k = \frac{1}{1 - \frac{\partial\Sigma'}{\partial\omega}}$, and moreover the computed Z'_k would be the same as in Eq. (S.3). Including $a_{\mathcal{G}}$ in the definition of Σ is a convenience employed for two reasons. First, it separates the effects of high and low energy physics formally. The factor $a_{\mathcal{G}}$ in Eq. (S.2) represents an overall depletion of the lower Hubbard band (due to excitations at scale U in a Hubbard model) and the term $\frac{\partial\Sigma_{DM}}{\partial\omega}$ in the denominator accounts for the depletion of the QP by low frequency FL effects. Secondly, introducing $a_{\mathcal{G}}$ results in a self energy Σ_{DM} that reaches a constant at high frequency, unlike the Dyson form given above with Z' which grows indefinitely.

Numerics are performed at finite temperature and the T=0 value of $\frac{\partial\Sigma}{\partial\omega}$ is obtained by extrapolation of the finite T data. It is found that Z_k falls quickly with density as plotted in Fig. (15). Z_k is always somewhat less then $1 - n$ decreasing roughly linearly with density. At the highest densities, near the limits of this theory, it begins to flatten. Thus, a Mott transition is absent in the $O(\lambda^2)$ theory.

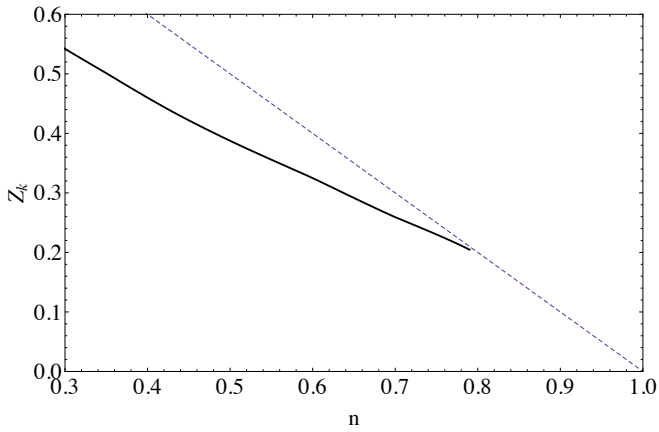

FIG. 15. The QP weight Z_{k_F} is plotted as a function of density. Z_{k_F} decreases with increased density, similar to (1-n) (which is depicted as a dotted line) but somewhat less. The incoherent spectral contribution is therefore already ~ 4 times greater than the QP part at $n \sim .7$, and this ratio appears to increase further near half filling.

FLOWCHART OF THE ITERATIVE PROCESS

Here we summarize the process by which numerical self consistency is achieved. The self consistency loop proceeds as follows.

1. Initialize all quantities to those of the Fermi gas: $\boldsymbol{\mu}' = \boldsymbol{\mu}_0$, $\rho_\Psi = \rho_{\overline{\Phi}} = 0$, u_0 is set to a plausible value of 2t.

2. Build $\rho_{\mathbf{g}}$ from latest instance of $\boldsymbol{\mu}'$, $\overline{\Phi}$.

3. Calculate $\rho_{\overline{\Phi}}$ from latest instance of $\rho_{\mathbf{g}}$ and u_0. Obtain the real part via Hilbert transform.

4. Calculate new $\boldsymbol{\mu}'$ using a bisection root finder.

5. Repeat steps 2-4 until $\boldsymbol{\mu}'$ and $\rho_{\overline{\Phi}}$ have converged to specified tolerance.

6. Calculate ρ_{Ψ} from latest $\rho_{\mathbf{g}}$ and u_0. Obtain real part through Hilbert transform.

7. Calculate $\sum_k \Psi(k)\mathbf{g}(k)$ and recalculate u_0 with a root finder.

8. Return to Step 2 and repeat loop. Continue to the next step only when u_0 has converged to specified tolerance.

9. Calculate $\rho_{\mathcal{G}}$.

The most computationally expensive step in this loop is the double integration for $\rho_{\overline{\Phi}}$. If computed by a direct summation the computational time required would scale as $N_s^2 N_\omega^2$. Furthermore, this slow step is on the inner most loop so it is repeated many times to find self consistent values of $\boldsymbol{\mu}$ and u_0. This leads to unacceptably slow convergence for any reasonable system size. Noting that the summation has the form of a convolution we can make use of FFT routines to calculate $\rho_{\overline{\Phi}}$ with linear scaling in $N_s N_\omega$. This allows us to reach significantly larger systems and lower temperatures than would be possible by a direct approach. The next bottleneck in this flowchart is the calculation of the Hilbert transforms. These can also be made fast through a judicious use of FFT routines. Thus, by using this approach we obtain a scheme which can calculate the full frequency and momentum dependence of $\rho_{\mathcal{G}}$ for lattices of substantial size, $N_s \sim 2000$ at temperatures as low as 30K.

Is it useful to discuss the tolerances set on the Lagrange multipliers. $\boldsymbol{\mu}$ is obtained to a relative precision of 10^{-5}. This is significantly more accurate than is required to satisfy the particle sum rule to within a tenth of a percent. However, we find empirically that this strict convergence criterion for $\boldsymbol{\mu}$ can not be satisfied until the spectral function $\rho_{\overline{\Phi}}$ is also well converged. Thus, if $\boldsymbol{\mu}$ has successfully converged to this tolerance we can be sure the $\rho_{\overline{\Phi}}$ is also well converged. The convergence criterion on u_0 requires the sum rule $\sum \Psi(k)g(k) = \frac{n^2}{4}(1-\frac{n}{2})$ to be satisfied to less than 10^{-4}. Again, this is overkill as it concerns the particle density alone. However, u_0 appears explicitly in $\bar{\Phi}$ and Ψ. The chosen convergence criterion is such that the final u_0 lands within $.01t$ of the exact value. This range is comparable to the smallest scales in our calculation, namely the frequency resolution $\Delta\omega$ and an implicit level broadening scale $\eta \to \Delta\omega$.

To exactly calculate the spectral functions, it is important to capture the entire range of the relevant frequencies. For non-interacting Fermions in 2 spatial dimensions this requires a frequency window no larger than 8t. However, the spectral functions $\rho_{\overline{\Phi}}$ and ρ_{Ψ} have long tails which extend to much higher frequency even though the renormalized QP bandwidth may be much narrower than the bare band. Thus it is important to determine empirically what range of frequency is sufficient to capture the full support of the spectral function. As mentioned before, we employ a frequency grid which extends over the range $|\omega| < 15t$, nearly four times the bare bandwidth, and find that this suffices to capture the support of all functions that arise.

FAST FOURIER TRANSFORMS FOR EVALUATING CONVOLUTIONS

The use of FFTs vastly reduces the time taken to compute the frequency and momentum sums. Each term of $\rho_{\overline{\Phi}}$ and ρ_{Ψ} is a convolution of 3 $\mathbf{g}$'s and has a form which is very similar to the particle-hole bubble diagrams familiar from a second-order perturbation treatment of the Hubbard model in U/t.

$$\Sigma(k)_{2^{nd}} \sim \sum_{pq} G(p)G(q)G(p+q-k); \quad \Sigma(i,j) \propto G(i,j)^2 G(j,i) \tag{S.4}$$

where $i = \vec{R}_i, \tau_i$ is a space time point. The convolution in Fourier space is a simple product in the space time domain and hence the real space version is advantageous. This is the well-known core idea of the FFT technique, where the time savings arise since the Fourier transforms are performed in $N \log N$ steps rather than N^2 (here $N = N_s N_\omega$). The ECFL "self energies", Ψ and Φ have the same frequency convolution structure of $\Sigma(k)_{2^{nd}}$ which appears only through the frequency arguments of $\mathbf{g}$. However, the $\rho_{\overline{\Phi}}$ and ρ_{Ψ} equations suffer from the presence of momentum-dependent decorations which render them not technically convolutions. Nonetheless we can use FFT routines to solve these summations. The strategy is to break up the integral into elementary pieces that do have the form of a convolution. We then avoid the need to do one large integral with quadratic complexity by doing many (≈ 70) small FFT's of linear complexity.

To accomplish this we define several $\mathbf{gg}$ correlation functions which are similar to particle-hole bubbles.

$$\chi_0(Q) = \sum_q \mathbf{g}(q)\mathbf{g}(q+Q); \; \chi_1(Q) = \sum_q \varepsilon_q \mathbf{g}(q)\mathbf{g}(q+Q)$$

$$\chi_2(Q) = \sum_q \varepsilon_{q+Q} \mathbf{g}(q)\mathbf{g}(q+Q); \; \chi_3(Q) = \sum_q \varepsilon_{q+Q}^2 \mathbf{g}(q)\mathbf{g}(q+Q)$$

each of which is a convolution in both frequency and momentum with a spectral function which can be calculated by FFT in linear time.

With these correlation functions every $\mathbf{ggg}$ term (except one to be discussed later) found in Ψ and $\overline{\Phi}$ can be written in the form

$$B_{\mathbf{ggg}}(k) = F_1(k) \sum_p F_2(p)\mathbf{g}(p)\chi_n(p-k)F_3(p-k). \tag{S.5}$$

where F_1,F_2, and F_3 are each functions of momentum only and their arguments are carefully matched with the arguments of $B_{\mathbf{ggg}}$, $\mathbf{g}$, and χ_n as they appear in the integral such that all factors fit the form of a convolution in both momentum and frequency. In this way we can massage every term of $\rho_{\overline{\Phi}}$ into a convolution of one $\mathbf{g}$ and a χ_n rather than three $\mathbf{g}$'s as originally written. There is one term in this problem which cannot be treated in this way because the argument matching of Eq. (S.5) cannot be achieved in such a simple way. This problem term looks like

$$\overline{\Phi}_{JJ}(k) = \sum_{pq} J_{q-k} J_{p-k} \mathbf{g}(p) \mathbf{g}(q) \mathbf{g}(p+q-k).$$

Nonetheless, this term can be treated by the FFT approach if the factor J_{q-k} is broken up using angle addition identities. This is accomplished without difficulty because the locality of J_{ij} ensures that J_k is composed of a small number of Fourier components.

In defining the Fourier transforms, we need to extend the frequency functions to infinity, since it is only then that the frequency convolutions become products in the time domain. Recall that our frequency integrals have been discretized onto N_ω frequency bins which cover the support of our spectral functions. In extending the discretized frequency summations to infinity, we follow the standard procedure of padding the N_ω frequency bins with an equal number of frequency bins with value zero. By a simple exercise one can verify that padding finite data in this way allows an application of the periodic FFT in such a way that the result of the infinite transform is reproduced. No such considerations are required for the momentum sums which are by definition periodic and discrete, making them naturally suited to treatment by FFT.

The Hilbert transform is formally a convolution and can therefore be solved with the advantages of the FFT routines. Once again, however, we face the problem that this convolution is a non-periodic frequency integral. Furthermore, the Hilbert kernel $\frac{1}{\omega}$, unlike other spectral functions with a compact support, falls off very slowly at large frequencies so the padding trick from the $\mathbf{g}\chi$ convolutions will not work well in this case. It is found that the use of FFT's to calculate a Hilbert transform will always introduce some error. Fortunately, this error can be controlled by increasing the length of padding used. In our code we use a frequency padding of $8N_\omega$ for the Hilbert transforms. This relegates the error of the real parts of the various functions to very high frequency, far beyond the compact support of the spectral functions. The error introduced is therefore negligible.